

# Advancements in Afterbody Radiative Heating Simulations for Earth Entry

Christopher O. Johnston<sup>\*</sup>

*NASA Langley Research Center, Hampton, VA 23681*

Marco Panesi<sup>†</sup>

*University of Illinois at Urbana-Champaign, Urbana, IL 61801*

and

Aaron M. Brandis<sup>‡</sup>

*AMA Inc at NASA Ames, Mountain View, CA 94035*

Four advancements to the simulation of backshell radiative heating for Earth entry are presented. The first of these is the development of a flowfield model that treats electronic levels of the dominant backshell radiator, N, as individual species. This is shown to allow improvements in the modeling of electron-ion recombination and two-temperature modeling, which are shown to increase backshell radiative heating by 10 to 40%. By computing the electronic state populations of N within the flowfield solver, instead of through the quasi-steady state approximation in the radiation code, the coupling of radiative transition rates to the species continuity equations for the levels of N, including the impact of non-local absorption, becomes feasible. Implementation of this additional level of coupling between the flowfield and radiation codes represents the second advancement presented in this work, which is shown to increase the backshell radiation by another 10 to 50%. The impact of radiative transition rates due to non-local absorption indicates the importance of accurate radiation transport in the relatively complex flow geometry of the backshell. This motivates the third advancement, which is the development of a ray-tracing radiation transport approach to compute the radiative transition rates and divergence of the radiative flux at every point for coupling to the flowfield, therefore allowing the accuracy of the commonly applied tangent-slab approximation to be assessed for radiative source terms. For the sphere considered at lunar-return conditions, the tangent-slab approximation is shown to provide a sufficient level of accuracy for the radiative source terms, even for backshell cases. This is in contrast to the agreement between the two approaches for computing the radiative flux to the surface, which differ by up to 40%. The final advancement presented is the development of a nonequilibrium model for NO radiation, which provides significant backshell radiation at velocities below 10 km/s. The developed model reduces the nonequilibrium NO radiation by 50% relative to the previous model.

## I. Introduction

Considering Earth entry at velocities greater than 8 km/s, a recent study<sup>1</sup> showed the potential for significant radiative heating along the backshell or afterbody surface, with values of similar magnitude to the convective heating. Although this afterbody radiative heating component was ignored in previous NASA designs without consequence, this was likely due to intentional over-design for Apollo<sup>2</sup> or the factor of 3.5 applied to the fully-catalytic convective heating for Stardust.<sup>3</sup> As afterbody convective heating values used for design become more aggressive with partially catalytic convective heating models, the importance of accurately modeling the afterbody radiation increases.

---

<sup>\*</sup>Aerospace Engineer

<sup>†</sup>Assistant Professor, AIAA Professional Member

<sup>‡</sup>Associate Research Scientist, AIAA Senior Member

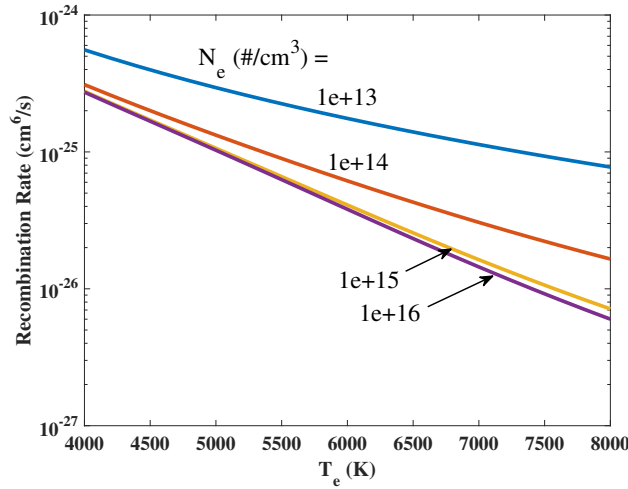


Figure 1: Recombination rate for atomic nitrogen at various electron number densities.

A distinct characteristic of afterbody radiation is that it is driven by a nonequilibrium expanding flow, where the rate of recombination of electrons and atomic ions governs the magnitude of the radiation. The faster the rate of recombination, the lower the radiation. This sensitivity to the recombination rate leads to numerous modeling challenges, two of which are identified and addressed in this work. The first challenge is that the recombination rates for atomic ions are dependent on the population of the upper electronic states of the associated neutral atom, which are themselves dependent on the electron number density and electron temperature, as well as the magnitude of local radiative emission and absorption.<sup>4</sup> This is shown in Figure 1, which compares the recombination rate for atomic nitrogen, computed from the present non-Boltzmann model (using escape factors presented later), for a range of electron number densities. For electron number densities below  $1 \times 10^{14} \text{ cm}^{-3}$ , which exist for most backshell conditions of interest, the recombination rate is seen to be a strong function of electron number density, as well as temperature. This complex dependency is not captured in conventional flowfield simulations, where the recombination rate is only a function of temperature. The second challenge is that the relatively complex geometry of afterbody flow makes questionable the validity of the typically applied tangent-slab approximation for the radiative source terms, which are required, as mentioned above, for predicting the electronic state populations.

A significant challenge not addressed in this work is the accuracy of the non-Boltzmann rate model for electron-impact excitation and ionization, which is shown by West et al.<sup>5</sup> to represent significant uncertainties to the backshell radiation. An associated paper by Lopez et al.<sup>6</sup> will examine the status of these rate models.

The present work addresses the first of the above challenges in Section II through the development of a flowfield model that treats electronic states of N as individual species in the flowfield, therefore allowing the dependency of the recombination rate on electron number density and radiative processes to be captured. As discussed in Section III, this state-specific model also results in improvements in the two-temperature model. Sections IV and V present the impact of the state-specific model, through comparisons with the conventional approach, for a Stardust and lunar-return case, respectively. The second of the identified challenges is addressed in Section VI, through the development of a ray-tracing approach for computing radiative source terms, which allows the tangent-slab approximation to be removed. This ray-tracing approach computes both the divergence of the radiative flux, required by the energy equations, as well as the absorption rate for each atomic line, required by the state-specific model. Finally, Section VII presents a nonequilibrium model for NO emission, which is identified as a significant backshell radiation contributor.

## II. State-Specific Flowfield Model for N

This section presents the state-specific flowfield model developed for N. To allow electronic states of N to be treated as individual species in the flowfield solver, the detailed 35 level model developed by Johnston et al.<sup>7</sup> is reduced to a more manageable 7 level model using the approach developed by Panesi and Lani.<sup>8</sup>

The grouping applied to the present model is defined in Table 1, where the grouped energy is defined as:

$$E_{i'} = \frac{\sum_{i \in G_{i'}} g_i E_i}{g_k} \quad (1)$$

The convention of this paper is that grouped levels are identified with a prime, such as  $i'$ , while individual levels are not. The individual levels within a group are assumed to follow a Boltzmann distribution, which results in the following relationship between the group and individual number density:

$$N_i = N_{i'} \frac{g_i}{Q_{i'}} \exp \left[ -\frac{hc}{kT_e} (E_i - E_{i'}) \right] \quad (2)$$

where

$$Q_{i'} = \sum_{i \in G_{i'}} g_i \exp \left[ -\frac{hc}{kT_e} (E_i - E_{i'}) \right] \quad (3)$$

To model the 7 grouped number densities,  $N_{i'}$ , as individual species within the flowfield solver, rate models for collisional and radiative processes are required. Development of these models are discussed in the following two subsections, while the third subsection discusses the implementation of these models in the LAURA/HARA code. Note that this implementation also requires modifications to the two-temperature model. These modifications are discussed in Section III.

**Table 1: Details of the grouped level model for N.**

Grouped Level, k	Individual Levels, $G_k$	$E_k$ (eV)	$g_k$
1	1	0.0	4
2	2	2.384	10
3	3	3.576	6
4	4 - 6	10.64	30
5	7 - 13	11.95	64
6	14 - 27	13.08	162
7	28 - 35	14.29	6578

## A. Collisional Processes

Following Panesi and Lani,<sup>8</sup> the electron-impact excitation rate between a lower grouped level  $i'$  and upper grouped level  $j'$ , is written in terms of the rates between ungrouped levels  $i$  and  $j$  as follows:

$$k_{i'j'}^{ex} = \sum_{j \in G_{j'}} \sum_{i \in G_{i'}} \frac{k_{ij}^{ex} g_i}{Q_{i'}} \exp \left[ -\frac{hc}{kT_e} (E_i - E_{i'}) \right] \quad (4)$$

The backwards rate for this process is written in terms of the forward rate and the equilibrium constant:

$$k_{j'i'}^{ex} = \frac{k_{i'j'}^{ex}}{K_{c,i'j'}^{ex}} \quad (5)$$

where the equilibrium constant is:

$$K_{c,i'j'}^{ex} = \frac{Q_{j'}}{Q_{i'}} \exp \left[ -\frac{hc}{kT_e} (E_{j'} - E_{i'}) \right] \quad (6)$$

Using the rates from the 35 level model developed by Johnston et al.,<sup>7</sup> the grouped rates were computed and curve fit to the following form:

$$k_{i'j'}^{ex} = AT_e^n e^{-E/T_e} \quad (7)$$

while the equilibrium constant was fit to the following:

$$K_{c,i'j'}^{ex} = e^{(G_1/z + G_2 + G_3 \log(z) + G_4 z + G_5 z^2)} \quad (8)$$

The coefficients for these curve-fits are listed in Table 3 of the appendix.

For an electron-impact ionization process from a grouped level  $i'$ , the grouped forward rate is computed as

$$k_{i'}^{ion} = \sum_{i \in G_{i'}} \frac{k_i^{ion} g_i}{Q_{i'}} \exp \left[ -\frac{hc}{kT_e} (E_{ionize} - E_{i'}) \right] \quad (9)$$

The recombination rate is computed using the equilibrium constant, which is written as:

$$K_{c,i'}^{ion} = \frac{2Q_+}{Q_{i'}} \left( \frac{2\pi m k T_e}{h^2} \right)^{3/2} \exp \left[ -\frac{hc(E_{ionize} - E_{i'})}{kT_e} \right] \quad (10)$$

The ionization rate and equilibrium constant are curve-fit to the form of Eqs. 7 and 8, respectively. The coefficients for these curve-fits are listed in Table 4.

In addition to these electron-impact excitation and electron-impact ionization processes, Tables 5 and 6 in the Appendix present the rates applied for other processes. For the state-specific results presented in this paper, instances of N in Tables 5 and 6 are replaced by the first grouped level of N, and the electron-impact ionization rate for N in Table 6 is not applied.

## B. Radiative Processes

For each bound-bound radiative transition between upper level  $j$  and lower level  $i$ , the transition rate from  $j$  to  $i$ , resulting from spontaneous emission from  $j$ , is written as:

$$k_{ji}^{em} = A_{ji} \quad (11)$$

where  $A_{ji}$  is the Einstein coefficient for the transition, which is independent of temperature and number density. Transitions in the opposite direction, between lower level  $i$  and upper level  $j$ , are dependent on absorption of the radiative intensity resulting from the entire flowfield ( $I_\nu$ ).

$$k_{ij}^{ab} = \int_0^\infty \frac{g_j b_\nu A_{ji} c^4 \int_{4\pi} I_\nu d\Psi}{8\pi h \nu^5} d\nu \quad (12)$$

The evaluation of this equation for a variable property tangent-slab is presented by Johnston,<sup>9</sup> while Section VI of the present paper discusses the application of a rigorous ray-tracing approach. Both the tangent-slab and ray-tracing approaches are computationally expensive because this term must be evaluated for every atomic line at every frequency and spatial point. Furthermore, treating this term requires numerous iterations due to its dependence on the rest of the flowfield.

Because of the difficulty in evaluating Eq. (12), this term is commonly approximated using the escape factor approach. This approach assumes a constant property sphere around the point of interest, and no interaction between overlapping atomic lines. With these assumptions, Eq. (12) reduces to the following

$$k_{ij}^{ab} = A_{ji} \frac{N_j}{N_i} (1 - EF_{ij}) \quad (13)$$

where the escape factor,  $EF_{ij}$ , is defined as

$$EF_{ij} = \int_0^\infty \exp(-\kappa_{\nu,ij} \Delta z) d\nu \quad (14)$$

For optically thin lines,  $EF_{ij}$  is equal to 1.0, while for optically-thick lines, such as those in the VUV,  $EF_{ij}$  is close to 0.0. Note that Eq. (14) does not allow for negative  $EF_{ij}$  values.

Even though Eq. (12) does not explicitly use  $EF_{ij}$  values, they may be computed as a post-processing step as follows:

$$EF_{ij} = 1 - \frac{k_{ij}^{ab}}{k_{ji}^{em}} \frac{N_i}{N_j} \quad (15)$$

Comparing  $EF_{ij}$  values from the approximate and detailed approaches will provide insight into the impact of the non-local absorption term in Eq. (12), which represents the fundamental difference between the two approaches.

The above equations for radiative processes are written for the non-grouped electronic levels  $i$  and  $j$ . To convert these terms to transitions between grouped levels  $i'$  and  $j'$ , as required for the state-specific flowfield model, the following equations are applied:

$$k_{j'i'}^{em} = \sum_{i \in G_{i'}} \sum_{j \in G_{j'}} \frac{k_{ji}^{em} g_j}{Q_{j'}} \exp \left[ -\frac{hc}{kT_e} (E_j - E_{j'}) \right] \quad (16)$$

$$k_{i'j'}^{ab} = \sum_{j \in G_{j'}} \sum_{i \in G_{i'}} \frac{k_{ij}^{ab} g_i}{Q_{i'}} \exp \left[ -\frac{hc}{kT_e} (E_i - E_{i'}) \right] \quad (17)$$

Applying these equations to a flowfield condition representative of a lunar-return flowfield, Table 2 lists values for  $k_{j'i'}^{em} EF_{i'j'}$  and  $EF_{i'j'}$  for each grouped level transition. This table shows the wide variation in the magnitude of  $EF_{i'j'}$  for the various transitions. With the exception of the 6-5 transition, the largest  $k_{j'i'}^{em} EF_{i'j'}$  values are seen for transitions with a  $i'=3$  and  $j'$  larger than 3, which represent vacuum ultraviolet (VUV) transitions. Unlike transitions with  $i'$  equal to 1 or 2, which are deeper into the VUV, the  $EF_{i'j'}$  values for  $i'=3$  transitions are greater than 0.2. These relatively large  $EF_{i'j'}$  values for VUV transitions, particularly the 4-3 transition, will be shown later in this paper to have a significant impact on the radiative environment.

**Table 2: Radiative transition rates for the grouped N model at a backshell flowfield condition.**

$j'$	$i'$	$k_{j'i'}^{em} EF_{i'j'}$	$EF_{i'j'}$	$j'$	$i'$	$k_{j'i'}^{em} EF_{i'j'}$	$EF_{i'j'}$
4	1	7.6e+0	2.6e-8	6	4	6.3e+4	7.1e-1
4	2	1.8e+5	3.3e-3	6	5	9.5e+6	4.1e-1
4	3	6.6e+6	3.2e-1	7	1	9.6e+1	8.6e-5
5	2	7.9e+4	4.2e-3	7	2	5.5e+4	7.6e-2
5	3	1.2e+6	4.4e-1	7	3	6.6e+5	1.0e+0
5	4	4.2e+5	1.7e-2	7	4	3.1e+4	7.6e-1
6	1	7.9e+2	3.1e-5	7	5	8.3e+5	1.0e+0
6	2	7.0e+5	2.7e-2	7	6	3.8e+5	1.0e+0
6	3	6.4e+6	6.5e-1				

### C. Implementation of the State-Specific Model for N in LAURA/HARA

The implementation of the collisional transition rates, discussed in subsection A, within the LAURA/HARA code<sup>10</sup> is relatively straightforward. The species source term due to these collisions is written as:

$$\left( \frac{\partial N_{i'}}{\partial t} \right)_{col} = \sum_{j'=1}^m k_{j'i'}^{ex} N_{j'} N_e - \sum_{j'=1}^m k_{i'j'}^{ex} N_{i'} N_e - \sum_{j'=1}^m k_{i'}^{ion} N_{i'} N_e + \sum_{j'=1}^m \frac{k_{i'}^{ion}}{K_{c,i'}} N_+ N_e^2 \quad (18)$$

The rates in this equation are implemented analogously to conventional flowfield rates, with the 7 grouped levels of N identified within the code as “N\_i”, where ‘i’ is group number. The presence of the underscore differentiates the grouped level from conventional species. Note that transport properties for the grouped levels are assumed equal to N for the conventional model.

In contrast to the collisional transition rates, implementation of the radiative transition rates requires an advanced level of coupling between the LAURA flowfield code and HARA radiation code. Within the LAURA code, the following radiative source term is added to the species continuity equations:

$$\left( \frac{\partial N_{i'}}{\partial t} \right)_{rad} = \sum_{j'=i'+1}^m (k_{j'i'}^{em} N_{j'} - k_{i'j'}^{ab} N_{i'}) + \sum_{j'=1}^{i'-1} (k_{j'i'}^{ab} N_{j'} - k_{i'j'}^{em} N_{i'}) \quad (19)$$

The transition rates due to emission ( $k_{j'i'}^{em}$ ) and absorption ( $k_{i'j'}^{ab}$ ) are computed in HARA using Eqs. (11)-(17). These rates are then sent to LAURA for implementation in Eq. (19). After a defined number of LAURA flowfield iterations, typically around 5000, the rates are recomputed in HARA. This process is repeated until convergence. This represents an additional level of coupling between LAURA and HARA, as typically

only the divergence of the radiative flux is passed from HARA to LAURA. Furthermore, three options for computing  $k_{j'i'}^{ab}$  have been implemented: the “approximate EF” approach computes  $k_{j'i'}^{ab}$  using escape factors; the “detailed EF” approach computes  $k_{j'i'}^{ab}$  using Eq. (12) and the tangent-slab approximation; and the “ray-tracing” approach computes  $k_{j'i'}^{ab}$  using Eq. (12) and the ray-tracing capability discussed in Section VI. Note that, by removing the quasi-steady state computation for the population of the N levels in HARA, the state-specific approach makes feasible the detailed treatment of radiative transition rates using either the tangent-slab approximation or the ray-tracing approach.

### III. Required Modifications to the Two-Temperature Model

By modeling electronic states of N as individual species in the flowfield, therefore making their electronic energy independent of the flowfield vibrational-electronic temperature,  $T_{ve}$ , modifications are required to the definition of  $T_{ve}$  and its governing energy equation. The temperature  $T_{ve}$  is defined for the state-specific N flowfield assuming equilibration between the vibrational energy modes of all molecules, the free electron translational energy, and the bound electronic energy of atoms and molecules other than N. In other words,  $T_{ve}$  is defined identically to Gnoffo et al.,<sup>11</sup> except the bound electronic states of N are no longer governed by this temperature because they are treated as individual species in the species continuity equation, which determines the population of each electronic level. Note that these bound electronic states of N are included in the total energy equation.

The conservation equation for the energy governed by  $T_{ve}$  is written similarly to the conventional vibrational-electronic energy equation defined by Gnoffo et al. The “vibrational-electronic” source terms are written as

$$\text{Source Terms} = R_{V-T} + R_{e-T} + S_V + \Omega_I + \Omega_E + Q_{rad} \quad (20)$$

where the  $R_{V-T}$ ,  $R_{e-T}$ , and  $S_V$  terms are the vibrational-translation energy relaxation, electron-translational energy relaxation, and vibrational energy reactive source terms, respectively, and do not require modification. The modification of the other three terms are discussed below.

#### A. Electronic Energy Reactive Source Term

The  $\Omega_I$  term is the electronic energy reactive source term, which is written by Gnoffo et al.<sup>11</sup> as

$$\Omega_I = - \sum_{s=\text{ions}} \dot{n}_{e,s} I_s \quad (21)$$

where  $\dot{n}_{e,s}$  is the production rate of ion  $s$  from the respective electron-impact ionization reaction and  $I_s$  is the ionization energy between the associated neutral atom and the ion  $s$ . This term is present in the conventional two-temperature model because the heats of formation of ions (and all species) are not included in the vibrational-electronic enthalpy, even though the heats of formation of ions include electronic energy equal to  $I_s$ . This term therefore accounts for this electronic energy implied by the heat of formation and allows for  $I_s$  to be chosen as a value lower than that assuming ionization from the ground state. For the present modified approach, the form of this term is the same, but the meaning is different for N. Electron-impact ionization processes result in a transfer of energy between free-electrons and bound electronic states, which are in different energy pools for N (unlike the conventional case) and therefore required this energy exchange term. The value of  $I_s$  for each electronic state of N is applied, therefore avoiding the need to assume a value, as required in the conventional approach.

#### B. Electron-Impact Excitation Energy Exchange

The  $\Omega_E$  term is the electron-impact excitation energy exchange term, which accounts for energy exchange when the impact of free-electrons causes a change between two bound electronic levels of N. This term is written as

$$\Omega_E = - \sum_{i'=1}^{N_E-1} \sum_{j'=i}^{N_E} \dot{n}_{e,i',j'} (E_{j'} - E_{i'}) \quad (22)$$

where  $\dot{n}_{e,i',j'}$  is the electron-impact transition rate between lower level  $i'$  and upper level  $j'$ . Note that this term is not required in the convectional approach described by Gnoffo et al.<sup>11</sup> because bound electronic levels of N and free-electron translational energy are both governed by  $T_{ve}$ .

### C. Divergence of the Radiative Flux

The radiative source term for the total energy equation is the divergence of the radiative flux, which is written as:

$$Q_{rad} = 4\pi j_\nu - \kappa_\nu \int_{4\pi} I_\nu d\Psi \quad (23)$$

For the conventional two-temperature model, this term is also applied to the vibrational-electronic energy equation, as a result of all significant radiative transitions being between vibrational or electronic states. For the present state-specific N model, however, an altered radiative source term ( $Q_{rad}^{VE}$ ), which removes energy from bound-bound radiative transitions of N, is required for the vibrational-electronic energy equation. This term may be computed based on the radiative transition rates for N in Eqs. (11) - (17) as follows:

$$Q_{rad}^{VE} = Q_{rad} - \sum_{i'=1}^m \sum_{j'=i'+1}^m (k_{j'i'}^{em} N_{j'} - k_{i'j'}^{ab} N_{i'}) hc(E_{j'} - E_{i'}) \quad (24)$$

This representation is convenient because it avoids evaluating additional computationally expensive terms.

## IV. Impact of the State-Specific Model on Stardust at 46 s

This section examines the differences in the radiative environment, predicted by the conventional and state-specific approach, for the Stardust capsule at the 46 s trajectory point (11.69 km/s,  $1.05 \times 10^{-4}$  kg/m<sup>3</sup>). This case was considered in previous studies by Johnston and Brandis<sup>1</sup> and West et al.<sup>5</sup> Figure 2 defines the three lines-of-sight that will be studied throughout this section.

For each of these lines-of-sight (LOS), the temperatures,  $\Phi$ , and wall-directed radiative intensity resulting from the conventional and state-specific approaches are compared in Figs. 3–5. Note that  $\Phi$  was defined by Johnston and Brandis<sup>1</sup> as

$$\begin{aligned} \Phi &= \log_{10} \left( \frac{N_j^{SB}}{N_j^B} \right) \\ &= \log_{10} \left[ \frac{N_+ N_e}{N_a} \frac{Q_a}{2Q_+} \left( \frac{h^2}{2\pi m k T_{ve}} \right)^{3/2} \exp \left( \frac{hc}{k T_{ve}} E_{ionize} \right) \right] \end{aligned} \quad (25)$$

This value represents the order-of-magnitude difference between the Boltzmann and Saha-Boltzmann distributions for N. As discussed by Johnston and Brandis,<sup>1</sup> larger positive values of  $\Phi$  result in stronger N emission.

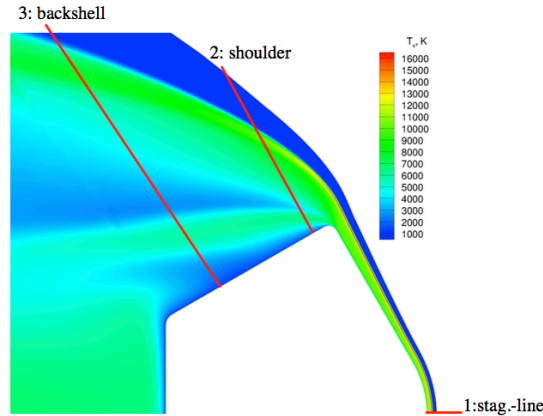


Figure 2: Line-of-sight definitions for the Stardust case.

Figure 3 presents these properties along the stagnation-line. This figure shows that the conventional and state-specific values agree in the equilibrium region of the flow (equilibrium flow is indicated by the  $\Phi$  values near 0), located between 0.2 and 0.8 cm. Notable differences are seen between the two approaches in the



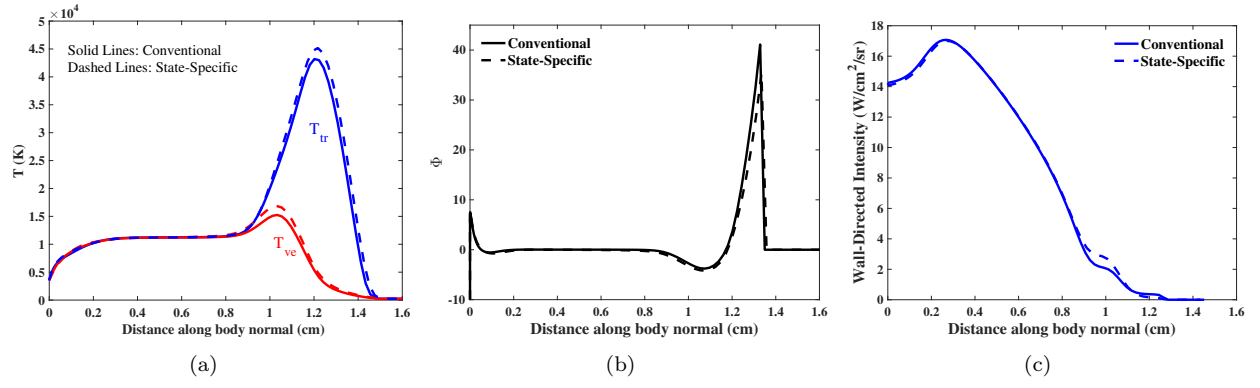


Figure 3: Profiles along LOS 1 (stagnation-line) for the Stardust case.

post-shock region of the flow, located above 0.8 cm, although these differences have a negligible impact on the radiative intensity reaching the surface, as shown in Fig. 3(c).

For the shoulder and backshell locations, Figs. 4 and 5 show significantly larger differences between the conventional and state-specific approaches than seen for the stagnation-line, which is expected because these lines-of-sight are located in regions of nonequilibrium, expanding flow. The temperature differences seen between the conventional and state-specific approaches are primarily the result of reduced vibrational-electronic specific heat for the state-specific approach (as discussed in Section III, this reduction is due to the removal of the N component). This smaller specific heat is less capable of offsetting the dominant translational-electron energy relaxation process between  $T_{ve}$  and  $T_{tr}$ , which is treated identically for the conventional and state-specific approaches. This relaxation process is unchanged between the two approaches because it is due to the frictional heating of electrons by heavy particles. It is therefore independent of the bound electronic energy of N, being instead dependent on the difference between the free-electron and translational temperatures. Consequently, the state-specific approach represents an improvement in two-temperature modeling, as the present differences seen between the conventional and state-specific temperatures indicate that the conventional approach's grouping of bound electronic energy of N and free-electron energy erroneously prevents stronger equilibration between the free-electron and heavy particle translational temperature.

This impact of the state-specific model on  $T_{ve}$  strongly influences radiative emission of N, as suggested by the dependence of  $\Phi$  on  $T_{ve}$  seen in Eq. (25). This equation shows that  $\Phi$  increases as  $T_{ve}$  decreases, which is also apparent in Figs. 4 and 5. Because, as noted previously, the radiative emission from N increases as  $\Phi$  increases, the counterintuitive result that the radiative emission from N increases as  $T_{ve}$  decreases is obtained. The physical interpretation for this relationship is that lower  $T_{ve}$  values, or more precisely lower free-electron translational temperatures, mean that the free-electrons have less kinetic energy for collisions required to depopulate the upper electronic levels of N. Once equilibration is achieved, meaning the Boltzmann and Saha-Boltzmann distributions are identical, then the typical relationship of increasing emission with increasing temperature is seen.

Figures 4(c) and 5(c) compare the wall-directed radiative intensity resulting from the conventional and state-specific approaches. Excluding the optically-thin and weakly emitting boundary layer region below 5 and 10 cm for the shoulder and backshell cases, respectively, differences in the intensity between the two approaches are seen to follow differences in  $\Phi$ . For both the shoulder and backshell cases, the state-specific approach predicts more radiative intensity reaching the surface. These larger values for the state-specific approach are the result of both the higher fidelity modeling of electron-ion recombination for N and the improved two-temperature modeling. When comparing the intensity profiles between the state-specific and conventional approaches, a region of larger emission by one approach is seen to relate to a larger  $\Phi$  value for that approach. This relates the discussion in the previous paragraphs, regarding the  $T_{ve}$  and  $\Phi$  comparisons between the state-specific and conventional approaches, to the actual radiation comparison. Note that these results apply the approximate escape factor (EF) approach discussed in Section II.B, which is applied identically in the conventional and state-specific approaches. The following paragraph will investigate the differences resulting from the approximate and detailed EF approaches.

As a result of the relatively low electron number density present in the shoulder and backshell regions of the flow, the radiative transition rates between electronic states discussed in Section II.B have a significant



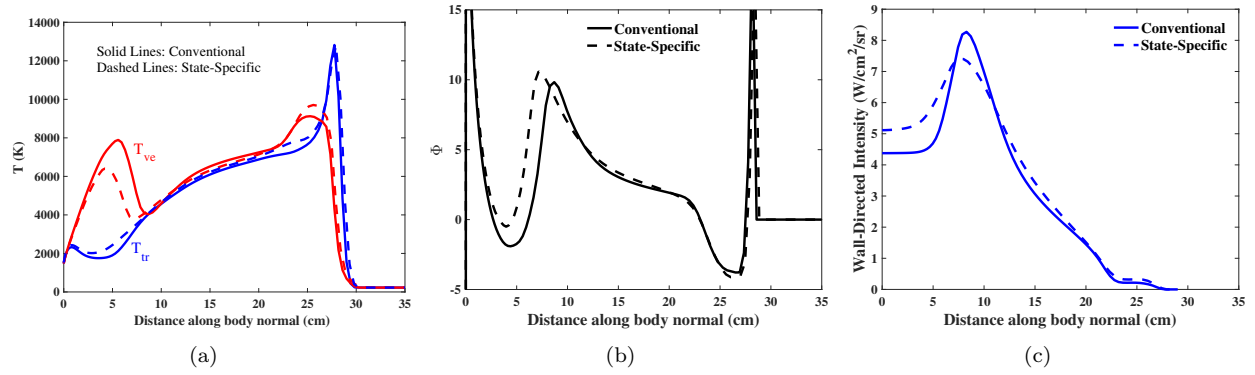


Figure 4: Profiles along LOS 2 (shoulder) for the Stardust case.

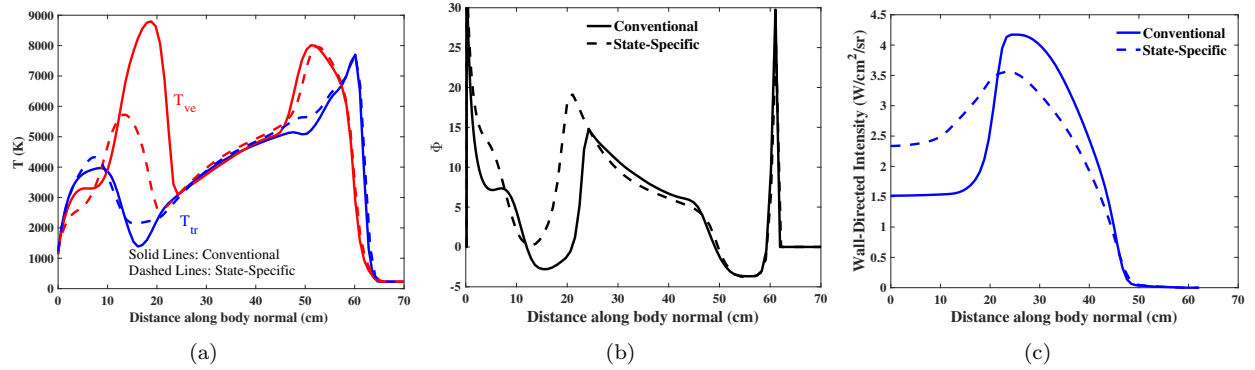


Figure 5: Profiles along LOS 3 (backshell) for the Stardust case.

impact on the upper level populations of N. Typical conventional flowfield simulations apply the approximate EF approach, represented by Eqs. (13) and (14), which, for each atomic line, computes an EF value at each spatial point in the flow based on only properties at that point. The more rigorous or detailed approach, represented by Eqs. (12) and (15), computes the transition rates at each spatial point based on the incoming radiative intensity from the surrounding flow. This approach is too computationally expensive when applied to the conventional approach, as a result of the required iterative QSS computations, so it has not been typically applied nor has its impact been assessed, with the exception of the study by Sohn et al.<sup>12</sup> for DSMC flows. However, its impact is potentially significant because the non-local nature is capable of capturing the impact of radiation from strongly emitting regions being absorbed by nearby weakly emitting regions, and therefore causing an increase in the local emission.

To examine the difference between approximate and detailed EF approaches, Figs. 6(a) and 7(a) compare the EF values for the dominant 4-3 transition for the shoulder and backshell lines-of-sight. Note that EF values for the approximate approach can only vary between 0.0 and 1.0, where a value of 1.0 indicates an optically-thin location, which provides the maximum depopulation of the upper level 4, and 0.0 indicates an optically thick location, which nullifies the radiative transition between levels 3 and 4. For the detailed approach, however, there is no lower limit for EF (although the upper limit remains 1.0). Negative values indicate that the transition rate due to absorption, which represents transitions from levels 3 to 4, is larger than the transition rate due to emission, which represents transitions from levels 4 to 3. Figures 6(a) and 7(a) show that the EF values are closest near the strongly emitting center of the shock layer. In addition to being strongly radiating, these regions have weaker gradients in temperatures and number densities, which make them more consistent with the approximations made in the derivation of the approximate approach. Outside of this center region, however, the detailed approach predicts significant absorption, represented by negative EF values, which the approximate approach is unable to model.

The consequence of the negative escape factors predicted by the detailed model, which repopulate the strongly emitting level 4, is apparent in the wall-directed radiative intensity profiles presented in Figs. 6(b) and 7(b). These figures compare the state-specific intensity resulting from the approximate and detailed EF

approaches (the result of the conventional approach, for which only the approximate result is available, is presented for reference). For the higher density shoulder line-of-sight, Fig. 6(b) shows only a 10% difference between the approximate and detailed EF approaches, which is primarily due to negative EF values around 5 cm. For the lower density backshell line-of-sight, Fig. 7(b) shows a nearly 40% difference between the two EF approaches, which is due to negative EF values near the shock and boundary layer.

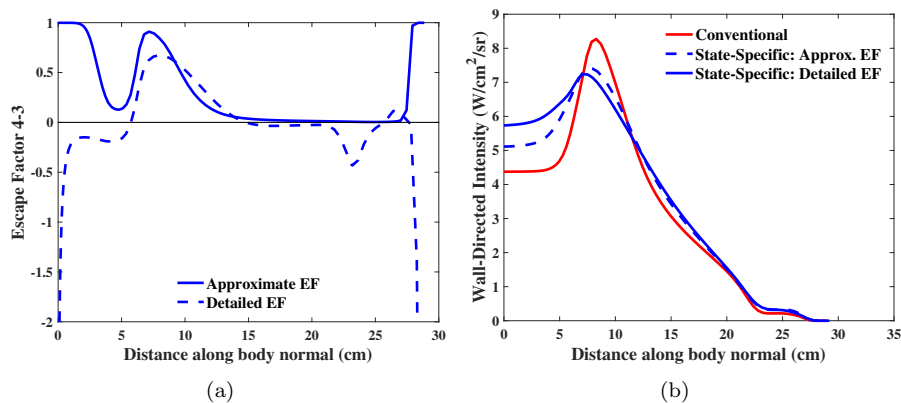


Figure 6: Impact of detailed escape factor treatment for shoulder line-of-sight.

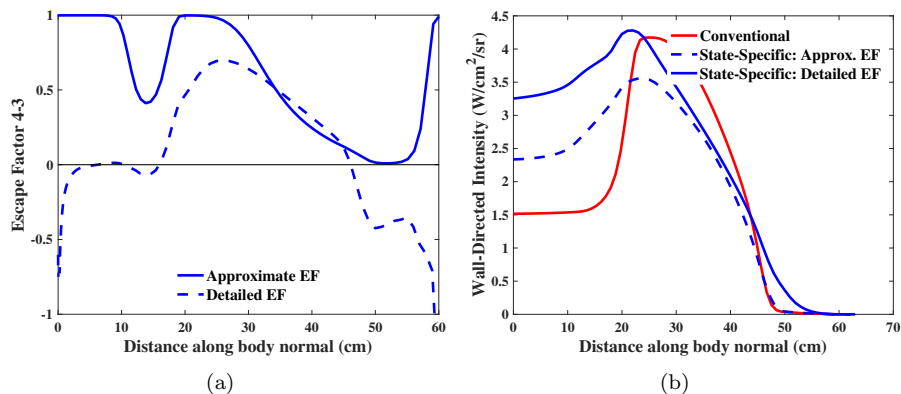


Figure 7: Impact of detailed escape factor treatment for backshell line-of-sight.

## V. Impact of the State-Specific Model on a Sphere at Lunar-Return Conditions

A 3-m radius sphere at a velocity of 10.5 km/s and density of  $2.73 \times 10^{-4}$  kg/m<sup>3</sup> (61 km altitude) is considered in this section. This condition is representative of a peak radiative heating trajectory point for a manned lunar return. Compared to the Stardust case presented in the previous section, which has a maximum radius of 0.41 m, the present case represents a larger vehicle at a lower velocity and higher density. The results presented for this case are in the same format used in the previous section for the Stardust case, and the comparisons are qualitatively similar, so the discussion is kept brief.

Figure 8 defines the lines-of-sight considered, while Figs. 9-11 compare the conventional and state-specific (with approximate EF) approaches along these lines of sight. As for the Stardust case, good agreement between the two approaches is seen for the stagnation-line. For the two other lines-of-sight, the stronger equilibration between the two temperatures is seen to result in larger radiative intensities for the state-specific case. Figures 12 and 13 show that, similar to the Stardust case, the detailed treatment of the escape factor results in a significant increase in the backshell radiation.

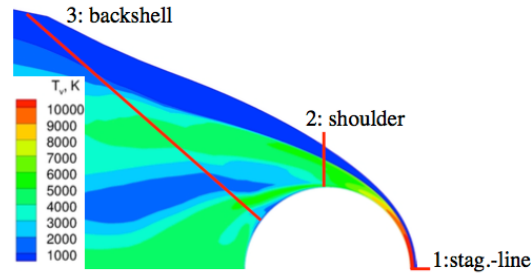


Figure 8: Line-of-sight definitions for the lunar-return sphere case.

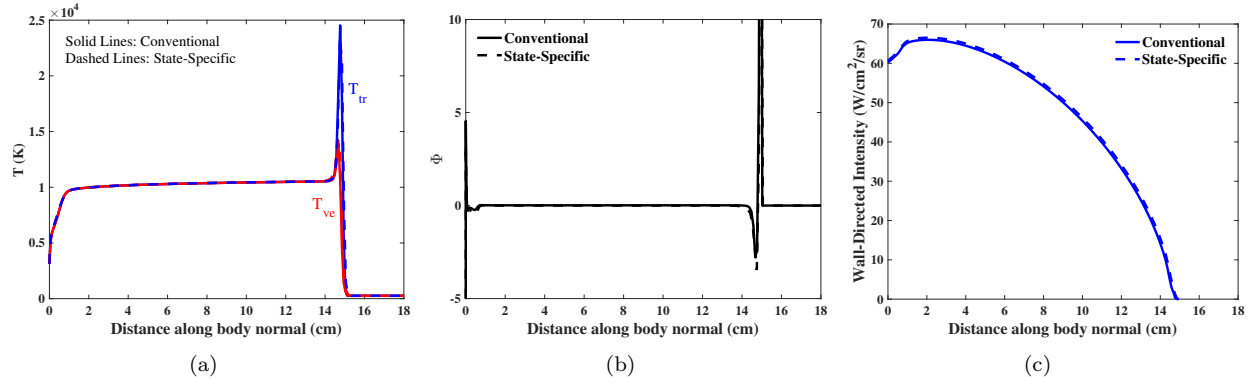


Figure 9: Profiles along LOS 1 (stagnation-line).

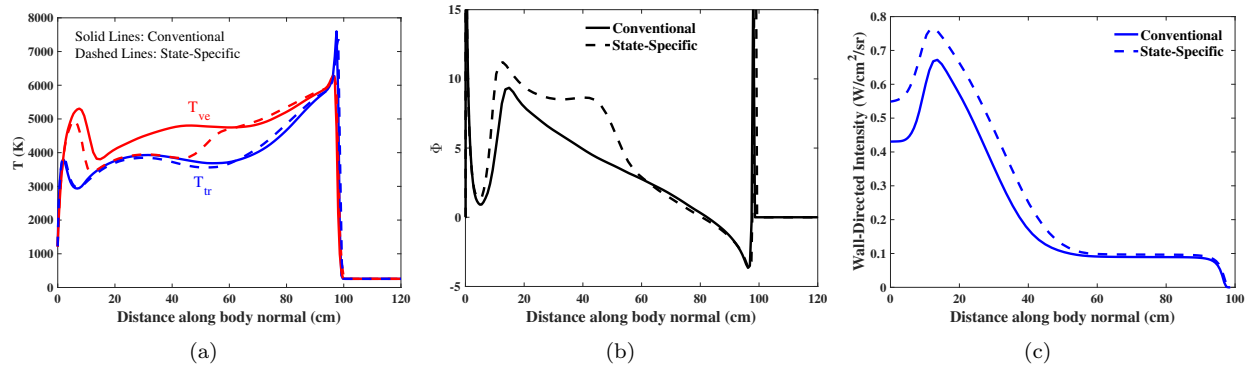


Figure 10: Profiles along LOS 2 (shoulder).

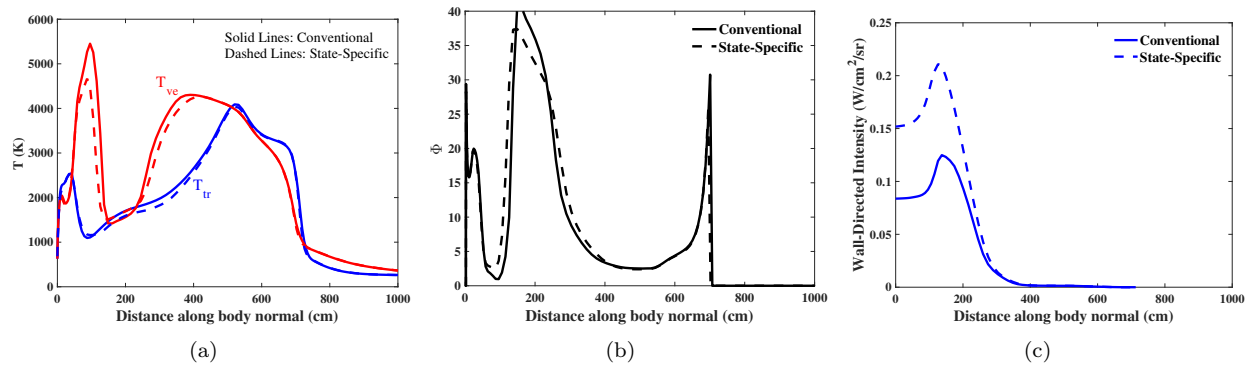


Figure 11: Profiles along LOS 3 (backshell).

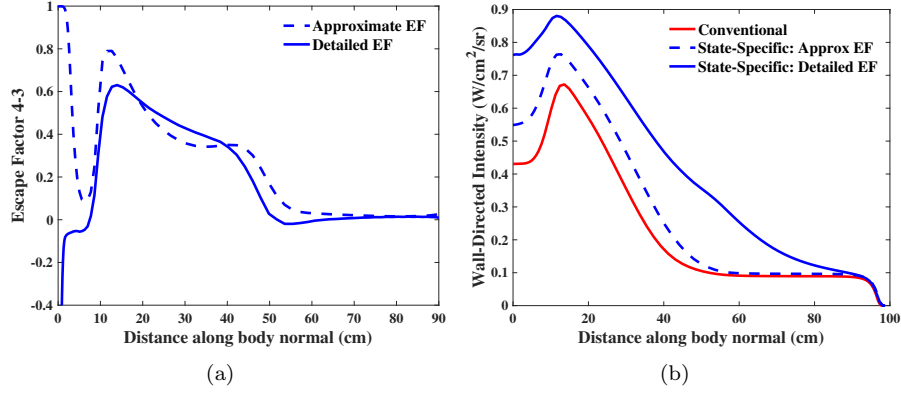


Figure 12: Impact of detailed escape factor treatment for shoulder line-of-sight.

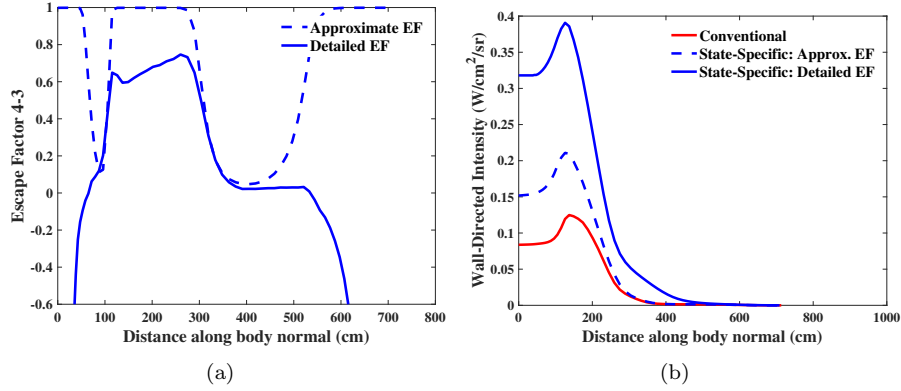


Figure 13: Impact of detailed escape factor treatment for backshell line-of-sight.

## VI. Impact of Three-Dimensional Radiative Transfer on Radiative Source Terms

In addition to the complexities discussed in the previous sections of modeling the nonequilibrium, expanding backshell flow, the radiative environment is complicated further by the non-tangent-slab geometry of this flow region, which makes questionable the application of the tangent-slab approximation for computing radiative source terms. These radiative source terms include both the divergence of the radiative flux ( $Q_{rad}$ ) and the absorption rate ( $k_{i,j}^{ab}$ ), the latter shown in Figs. 12 and 13 to have a significant impact on the backshell intensity.

Although the inadequacy of the tangent-slab approximation has been established for computing the radiative flux reaching the backshell surface,<sup>1,13</sup> resulting in over-predictions of up to 50%, it has not been confirmed that the radiative source terms resulting from the tangent-slab approximation introduce similarly large inaccuracies in the radiative flux reaching the surface. Note that removing the tangent-slab approximation for computing the surface radiative flux requires ray-tracing computations to points on the surface only, which increases the computational cost by roughly two orders-of-magnitude. Removing the tangent-slab approximation from the radiative source term computation, however, requires ray-tracing computations to essentially every point in the flowfield, which increases the computational cost by five orders-of-magnitude. This five orders-of-magnitude increase in computational cost is avoidable if the tangent-slab approach can be shown to sufficiently model the radiative source terms in the backshell flow. This question will be assessed in the present section through comparisons between the tangent-slab approximation and a recently developed ray-tracing capability.

For the lunar-return sphere considered in the previous section, Figs. 14 - 16 compare the tangent-slab and ray-tracing results for the three lines-of-sight defined in Fig. 8. These results are for the state-specific simulations, and the radiative source terms for both the ray-tracing and tangent-slab results have been

iterated until convergence. For each line-of-sight, the divergence of the radiative flux ( $Q_{rad}$ ), absorption rate between levels 3 and 4 of N ( $k_{3,4}^{ab}$ ), and wall-directed radiative intensity are compared.

Considering the stagnation-line in Fig. 14, relatively close agreement between the ray-tracing and tangent-slab results is seen for each of the quantities. Note the excellent agreement seen for  $Q_{rad}$ . This is unexpected because, as has been widely reported, the stagnation point radiative heating predicted by tangent-slab and ray-tracing typically disagree by 10-20% (the ray-tracing radiative heating (not shown) is 13% lower than the tangent-slab value for the present case). However, the wall-directed and shock-directed radiative flux predicted by tangent-slab result in canceling errors, which results in the good comparison for  $Q_{rad}$ .

Applying ray-tracing to evaluate the radiative heating (to the surface only), as a post-processing step, for the flowfield computed using tangent-slab radiative source terms results in agreement within 2% of the full ray-tracing result. This agreement is implied by the good agreement between the wall-directed intensity shown in Fig. 14(c), which also presents the result with radiative source terms set to zero (uncoupled) to show that the impact of these terms is significant. The agreement shown here between the ray-tracing and tangent-slab approaches provides valuable evidence that using the tangent-slab approximation for radiative source terms provides accurate coupled radiation flowfields in the stagnation region.

Such good agreement is not expected for the lines-of-sight presented in Figs. 15 and 16, which are located in less tangent-slab-like regions of the flow. Although there are noticeable differences between the ray-tracing and tangent-slab results for  $Q_{rad}$ , the agreement is better than expected. Larger differences are seen for  $k_{3,4}^{ab}$ , however, these differences are seen to have minimal impact on the radiative intensity. This agreement provides unexpected evidence that the tangent-slab approximation for radiative source terms results in minimal error for even non-tangent-slab-like regions of the flow.

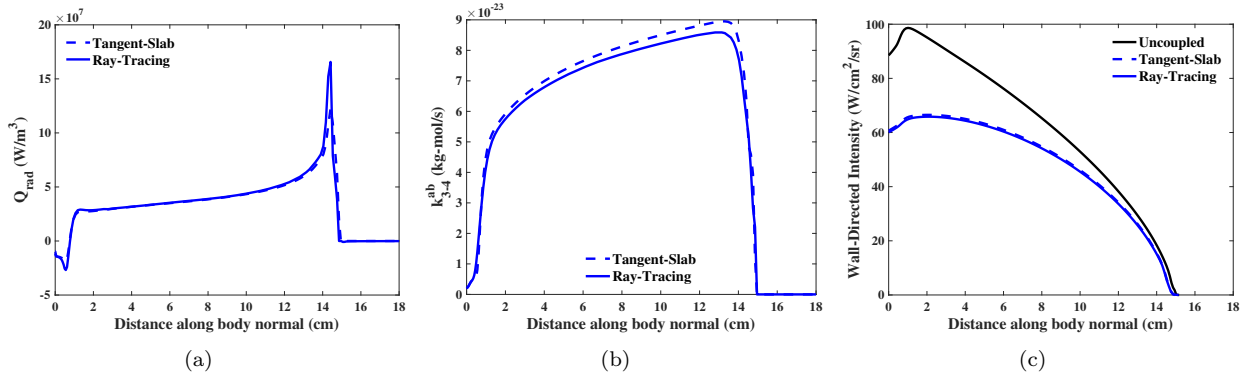


Figure 14: Profiles along LOS 1 (stagnation-line).

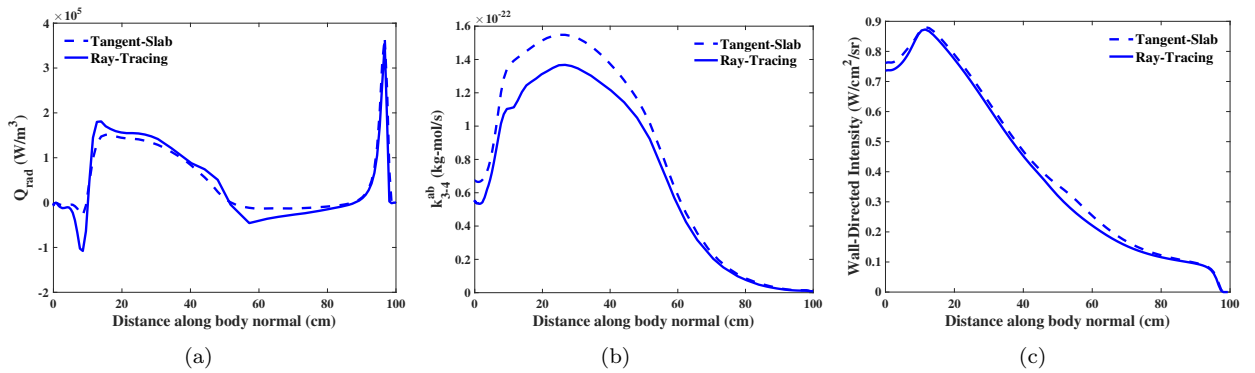


Figure 15: Profiles along LOS 2 (shoulder).

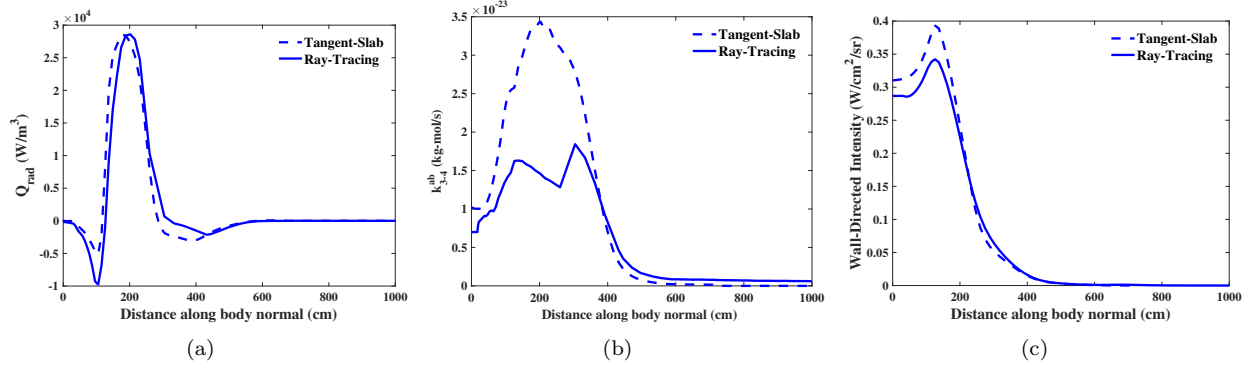


Figure 16: Profiles along LOS 3 (backshell).

## VII. Impact of Nonequilibrium NO Emission

The final subject addressed in this paper is the modeling of post-shock emission from NO band systems. Although nonequilibrium NO emission is typically associated with entry velocities below 10 km/s, it provides a noticeable contribution to backshell radiation at velocities greater than 10 km/s, as a result of the decreased angle between the velocity vector and the shock (making the velocity component normal to the shock lower than 10 km/s). Furthermore, NO emission provides the dominant backshell radiation component for entry velocities between 8 and 10 km/s. Although the backshell radiative heating is only on the order of 1 W/cm<sup>2</sup> at these velocities, typical lunar-return trajectories spend a longer time at these velocities than between 10 - 11 km/s, and therefore the contribution of these relatively low heat fluxes on the heat load is not negligible.

The non-Boltzmann NO rates applied previously in the HARA code were based on values provided by Park.<sup>14</sup> Using the same approach applied by Johnston and Brandis,<sup>15</sup> where the non-Boltzmann rates were tuned to match EAST measurements, a non-Boltzmann model was developed for NO. Details of the development of this model, and comparisons with measurements, are presented in Appendix C. This new model was applied for all cases presented previously in this paper.

The impact of the new NO non-Boltzmann model on the shoulder line-of-sight defined in Fig. 8 for a 9.5 and 10.5 km/s case, both at 61 km altitude, is presented in Fig. 17. The new model is seen to reduce the radiative intensity reaching the surface by 50% and 20% for the 9.5 and 10.5 km/s cases, respectively. The NO emission is seen as the sharp increase in intensity located near 100 cm. For both cases, this contribution is reduced by nearly half. This corresponds to the 50% reduction for the 9.5 km/s case because NO is the dominant radiator across the line-of-sight, while the 10.5 km/s case includes the atomic contribution below 40 cm, which reduces the percent impact of the NO model.

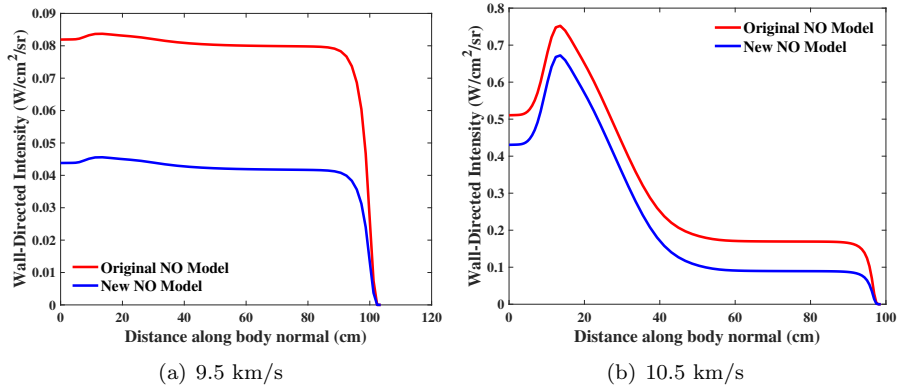


Figure 17: Impact of the new NO non-Boltzmann model on the shoulder line-of-sight.

## VIII. Conclusions

Four advancements to state-of-the-art radiative heating simulations are presented in this paper, with the aim of these advancements being the improvement of backshell radiative heating predictions. The first of these advancements is the development of a flowfield model that treats electronic states of N as individual species. This enables improvements in both the recombination rate of N and the two-temperature modeling, which result in 10 - 40% increase in the backshell radiation. The second advancement is the detailed treatment of radiative absorption on the non-Boltzmann model, representing detailed escape factors. The state-specific flowfield model allows for the detailed escape factor treatment with minimal increase in computational cost. For low density wake conditions, the detailed escape factor approach increases the radiation by up to 100%. This significant impact, which implies the backshell radiation is strongly dependent upon radiative transport dependent source terms, motivated the third advancement of ray-tracing radiation transport for radiative source terms. For the relatively simple axisymmetric hemisphere case considered, the differences between source terms predicted by the ray-tracing and tangent-slab approximation are shown to result in less than a 10% difference in the backshell radiation. Finally, the fourth advancement is the development of a non-Boltzmann model for NO based on EAST measurements. This new model results in a nearly 50% decrease in the NO emission relative to the previous model, which has a significant impact for velocities below 10 km/s.

## IX. Acknowledgments

The present work was funded by the NASA Space Technology Mission Directorate Entry Systems and Modeling (ESM) project, with tasks leads Michael Wright and Michael Barnhardt.

## References

- <sup>1</sup>Johnston, C. O. and Brandis, A. M., "Features of Afterbody Radiative Heating for Earth Entry," *Journal of Spacecraft & Rockets*, Vol. 52, No. 1, 2015, pp. 105–119.
- <sup>2</sup>Erb, R. B., Greenshields, D. H., and Chauvin, L. T., "Apollo Thermal Protection System Development," AIAA Paper 1968–1142, 1968.
- <sup>3</sup>Olynick, D., Chen, Y.-K., and Tauber, M. E., "Aerothermodynamics of the Stardust Sample Return Capsule," *Journal of Spacecraft & Rockets*, Vol. 36, No. 3, 1999, pp. 442–462.
- <sup>4</sup>Bourdon, A. and Vervisch, P., "Three-Body Recombination Rate of Atomic Nitrogen in Low Pressure Plasma Flows," *Physical Review E*, Vol. 54, No. 2, 1996, pp. 1888–1898.
- <sup>5</sup>West, T. K., Hosder, S., and Johnston, C. O., "Uncertainty and Sensitivity Analysis of Afterbody Radiative Heating Predictions for Earth Entry," AIAA Paper 2016–0738, 2016.
- <sup>6</sup>Lopez, B. and Panesi, M., "Study on Non-Boltzmann Models for Atomic Nitrogen," AIAA Paper 2015–XXXX, 2016.
- <sup>7</sup>Johnston, C. O., Hollis, B., and Sutton, K., "Non-Boltzmann Modeling for Air Shock Layers at Lunar Return Conditions," *Journal of Spacecraft & Rockets*, Vol. 45, Sep.-Oct. 2008, pp. 879–890.
- <sup>8</sup>Panesi, M. and Lani, A., "Collisional Radiative Coarse-Grain Model for Ionization in Air," *The Physics of Fluids*, Vol. 25, No. 057101, 2013.
- <sup>9</sup>Johnston, C. O., "Influence of Radiative Absorption on Non-Boltzmann Modeling for Mars Entry," *Journal of Thermophysics and Heat Transfer*, Vol. 28, No. 4, 2014, pp. 795–798.
- <sup>10</sup>Mazaheri, A., Gnoffo, P. A., Johnston, C. O., and Kleb, B., "LAURA Users Manual," NASA TM 2013-217800, 2013.
- <sup>11</sup>Gnoffo, P. A., Gupta, R. N., and Shinn, J. L., "Conservation Equations and Physical Models for Hypersonic Air Flows in Thermal and Chemical Nonequilibrium," NASA TP 2867, Feb. 1989.
- <sup>12</sup>Sohn, I., Li, Z., and Levin, D. A., "Effect of Nonlocal Vacuum Ultraviolet Radiation on Hypersonic Nonequilibrium Flow," *Journal of Thermophysics and Heat Transfer*, Vol. 26, No. 3, 2012, pp. 393–406.
- <sup>13</sup>Mazaheri, A., Johnston, C., and Sefidbakht, S., "Three-Dimensional Radiation Ray-Tracing for Shock Layer Radiative Heating Simulations," *Journal of Spacecraft & Rockets*, Vol. 50, No. 3, 2013, pp. 485–493.
- <sup>14</sup>Park, C., "Rate Parameters for Electronic Excitation of Diatomic Molecules II. Heavy Particle-Impact Processes," AIAA Paper 2008-1446, 2008.
- <sup>15</sup>Johnston, C. O. and Brandis, A. M., "Modeling of Nonequilibrium CO Fourth-Positive and CN Violet Emission in CO<sub>2</sub>-N<sub>2</sub> Gases," *Journal of Quantitative Spectroscopy and Radiative Transfer*, Vol. 149, 2014, pp. 303–317.
- <sup>16</sup>Bourdon, A. and Vervisch, P., "Study of Low-Pressure Nitrogen Plasma Boundary Layer over a Metallic Plate," *Physics of Plasmas*, Vol. 4, No. 11, 1997, pp. 4144–4157.
- <sup>17</sup>Fujita, K., Yamada, T., and Ishii, N., "Impacts of Ablation Gas Kinetics on Hyperbolic Entry Radiative Heating," AIAA Paper 2006-1185, Jan. 2006.
- <sup>18</sup>Park, C., *Nonequilibrium Hypersonic Aerothermodynamics*, Wiley, 1st ed., 1990.
- <sup>19</sup>Bose, D. and Candler, G. V., "Thermal Rate Constants of the O<sub>2</sub>+N $\leftrightarrow$ NO + O Reaction based on the <sup>2</sup>A' and <sup>4</sup>A' Potential Energy Surfaces," *Journal of Chemical Physics*, Vol. 107, 1997, pp. 6136–6145.



<sup>20</sup>Park, C., “Review of Chemical-Kinetic Problems for Future NASA Missions, I: Earth Entries,” *Journal of Thermophysics and Heat Transfer*, Vol. 7, No. 3, 1993, pp. 385–398.

<sup>21</sup>Teulet, P., Gonzalez, J. J., Mercado-Cabrera, A., Cressault, Y., and Gleizes, A., “One-Dimensional Hydro-Kinetic Modeling of the Decaying Arc in Air-PA66-Copper Mixtures: I. Chemical Kinetics, Thermodynamics, Transport and Radiative Properties,” *Journal of Physics D: Applied Physics*, Vol. 42, 2009, pp. 1–15.

<sup>22</sup>Gorelov, V. A., “Experimental and Numerical Study of Nonequilibrium Ultraviolet NO and N<sub>2</sub><sup>+</sup> Emission in a Shock-Layer,” *Journal of Thermophysics and Heat Transfer*, Vol. 12, 1998, pp. 172–179.

<sup>23</sup>Li, Z., Sohn, I., and Levin, D. A., “Modeling of Nitrogen Monoxide Formation and Radiation in Nonequilibrium Hypersonic Flows,” *Journal of Thermophysics and Heat Transfer*, Vol. 28, No. 3, 2014, pp. 365–380.

<sup>24</sup>Cruden, B. A., Martinez, R., Grinstead, J. H., and Olejniczak, J., “Simultaneous Vacuum Ultraviolet through Near IR Absolute Radiation Measurements with Spatiotemporal Resolution in an Electric Arc Shock Tube,” AIAA Paper 2009-4240, 2009.

## Appendix

### A. State-Specific Rates for N

Tables 3 and 4 present the coefficients for Eqs. (7) and (8) developed for the electron-impact excitation and ionization rates, respectively. These rates represent the state-specific model developed in the present work for N.

Table 3: Electron-impact excitation rates for N.

$i'$	$j'$	$A$	$n$	$E$	$G_1$	$G_2$	$G_3$	$G_4$	$G_5$
1	2	1.406e+13	5.571e-01	2.76780e+04	1.77636e-15	9.16291e-01	-2.93099e-14	-2.76780e+00	-4.08007e-15
1	3	2.324e+15	-1.475e-02	4.15131e+04	2.84217e-14	4.05465e-01	-6.75016e-14	-4.15131e+00	-4.88498e-15
1	4	2.085e+21	-1.136e+00	1.23544e+05	-1.05989e-01	1.91969e+00	-2.78234e-01	-1.21187e+01	1.41200e-02
1	5	9.717e+15	-3.703e-02	1.38746e+05	-4.04740e-02	2.72563e+00	-1.12245e-01	-1.37679e+01	1.04969e-02
1	6	2.992e+14	3.272e-01	1.51840e+05	-1.57976e-02	3.68556e+00	-4.23075e-02	-1.51463e+01	7.81791e-03
1	7	3.160e+17	-4.979e-01	1.65937e+05	8.76378e-02	7.50474e+00	2.42279e-01	-1.68200e+01	6.07758e-02
2	3	9.684e+14	2.191e-01	1.38351e+04	4.08562e-14	-5.10826e-01	7.63833e-14	-1.38351e+00	3.60822e-15
2	4	3.487e+17	-3.784e-01	9.58655e+04	-1.05989e-01	1.00340e+00	-2.78234e-01	-9.35085e+00	1.41200e-02
2	5	3.378e+16	-1.152e-01	1.11068e+05	-4.04740e-02	1.80934e+00	-1.12245e-01	-1.10001e+01	1.04969e-02
2	6	3.520e+15	1.218e-01	1.24162e+05	-1.57976e-02	2.76926e+00	-4.23075e-02	-1.23785e+01	7.81791e-03
2	7	5.085e+17	-4.992e-01	1.38259e+05	8.76378e-02	6.58845e+00	2.42279e-01	-1.40522e+01	6.07758e-02
3	4	2.758e+17	-3.356e-01	8.20304e+04	-1.05989e-01	1.51423e+00	-2.78234e-01	-7.96734e+00	1.41200e-02
3	5	2.224e+16	-7.572e-02	9.72332e+04	-4.04740e-02	2.32016e+00	-1.12245e-01	-9.61659e+00	1.04969e-02
3	6	2.858e+15	1.650e-01	1.10327e+05	-1.57976e-02	3.28009e+00	-4.23075e-02	-1.09950e+01	7.81791e-03
3	7	6.708e+17	-5.000e-01	1.24424e+05	8.76378e-02	7.09927e+00	2.42279e-01	-1.26687e+01	6.07758e-02
4	5	6.243e+16	2.514e-01	1.52027e+04	6.55146e-02	8.05935e-01	1.65989e-01	-1.64925e+00	-3.62308e-03
4	6	7.237e+15	3.224e-01	2.82967e+04	9.01909e-02	1.76586e+00	2.35927e-01	-3.02764e+00	-6.30205e-03
4	7	2.662e+18	-3.454e-01	4.23932e+04	1.93626e-01	5.58505e+00	5.20513e-01	-4.70136e+00	4.66559e-02
5	6	2.811e+17	2.011e-01	1.30940e+04	2.46764e-02	9.59928e-01	6.99376e-02	-1.37839e+00	-2.67897e-03
5	7	2.497e+19	-4.488e-01	2.71905e+04	1.28112e-01	4.77911e+00	3.54524e-01	-3.05211e+00	5.02790e-02
6	7	8.076e+20	-5.740e-01	1.40965e+04	1.03435e-01	3.81918e+00	2.84586e-01	-1.67372e+00	5.29579e-02

Table 4: Electron-impact ionization rates for N.

$i'$	$A$	$n$	$E$	$G_1$	$G_2$	$G_3$	$G_4$	$G_5$
1	1.241e+13	4.326e-01	1.68905e+05	1.23478e-01	-4.15111e+00	-1.57524e+00	-1.68239e+01	-6.60695e-03
2	1.334e+13	3.850e-01	1.41227e+05	1.23478e-01	-5.06740e+00	-1.57524e+00	-1.40561e+01	-6.60695e-03
3	2.061e+13	3.578e-01	1.27392e+05	1.23478e-01	-4.55658e+00	-1.57524e+00	-1.26726e+01	-6.60695e-03
4	3.019e+13	8.985e-01	4.53614e+04	2.29467e-01	-6.07080e+00	-1.29701e+00	-4.70525e+00	-2.07269e-02
5	1.487e+14	8.267e-01	3.01587e+04	1.63952e-01	-6.87674e+00	-1.46300e+00	-3.05600e+00	-1.71038e-02
6	1.260e+15	7.322e-01	1.70647e+04	1.39276e-01	-7.83667e+00	-1.53293e+00	-1.67761e+00	-1.44249e-02
7	5.018e+18	2.437e-01	2.96823e+03	3.58407e-02	-1.16559e+01	-1.81752e+00	-3.89284e-03	-6.73828e-02

## B. Flowfield Chemistry

Tables 5 and 6 present the flowfield chemistry applied in this work for the conventional flowfield cases. For the state-specific cases, the same rates are applied, except for the electron-impact ionization rate for N. Furthermore, the reactions involving N are replaced by the ground state of N, or level 1.

Table 5: Chemical kinetics for neutral species.

$i$	Reaction	$A_{f,i}$	$n_{f,i}$	$D_{f,i}$	$T_{f,i}$	Third Body, M	Ref.	$F_i$
1	$N_2 + M \leftrightarrow 2N + M$	8.6e+21	-1.60	1.132e+5	$T_a$	N, C, O	This Work	0.29
		6.0e+3	2.6	1.132e+5	$T_{ve}$	$e^-$	Bourdon et al. <sup>16</sup>	1.2e-5
		2.0e+21	-1.60	1.132e+5	$T_a$	others	This Work	0.29
2	$N_2 + O \leftrightarrow NO + N$	6.0e+13	0.1	3.80e+4	$T_{tr}$		Fujita et al. <sup>17</sup>	1.9
3	$NO + M \leftrightarrow N + O + M$	4.40e+16	0.00	7.55e+4	$T_a$	N, C, O, NO, CO <sub>2</sub>	Johnston and Brandis <sup>15</sup>	0.4
		2.0e+15	0.00	7.55e+4	$T_a$	others	Johnston and Brandis <sup>15</sup>	0.4
4	$O_2 + M \leftrightarrow 2O + M$	1.0e+22	-1.50	5.936e+04	$T_a$	N, C, O	Park <sup>18</sup>	1
		2.0e+21	-1.50	5.936e+04	$T_a$	others	Park <sup>18</sup>	1
5	$O_2 + N \leftrightarrow NO + O$	2.49e+9	1.18	4.01e+3	$T_{tr}$		Bose & Candler <sup>19</sup>	2.2

Table 6: Chemical kinetics for ionized species.

$i$	Reaction	$A_{f,i}$	$n_{f,i}$	$D_{f,i}$	$T_{f,i}$	Ref.	$F_i$	
6	$N + N \leftrightarrow N_2^+ + e^-$	4.40e+07	1.5	6.75e+4	$T_{tr}$	$T_{ve}$	Park <sup>20</sup>	1
7	$N + O \leftrightarrow NO^+ + e^-$	5.30e+12	0.0	3.19e+4	$T_{tr}$		Park et al. <sup>20</sup>	1
8	$N + e^- \leftrightarrow N^+ + 2e^-$	5e+21	-0.82	1.682e+5	$T_{ve}$	$T_{ve}$	This Work	0.2
9	$N^+ + N_2 \leftrightarrow N_2^+ + N$	4.00e+12	0.5	1.22e+4	$T_{tr}$	$T_{tr}$	This Work	4
10	$N_2 + O^+ \leftrightarrow N_2^+ + O$	9.10e+11	0.36	2.28e+4	$T_{tr}$	$T_{tr}$	Park <sup>18</sup>	1
11	$N_2 + e^- \leftrightarrow 2N + e^-$	6.0e+3	2.60	1.132e+5	$T_e$		Bourdon et al. <sup>16</sup>	1
12	$NO + O^+ \leftrightarrow N^+ + O_2$	1.40e+5	1.9	2.66e+4	$T_{tr}$	$T_{tr}$	Park <sup>18</sup>	1
13	$NO^+ + N \leftrightarrow N_2^+ + O$	7.20e+13	0.0	3.55e+4	$T_{tr}$	$T_{tr}$	Park <sup>18</sup>	1
14	$NO^+ + N \leftrightarrow O^+ + N_2$	3.40e+13	-1.08	1.28e+4	$T_{tr}$		Park <sup>18</sup>	1
15	$NO^+ + O \leftrightarrow N^+ + O_2$	1.00e+12	0.5	7.72e+4	$T_{tr}$	$T_{tr}$	Park <sup>18</sup>	1
16	$NO^+ + O \leftrightarrow O_2^+ + N$	7.20e+12	0.29	4.86e+4	$T_{tr}$		Park <sup>18</sup>	1
17	$NO^+ + O_2 \leftrightarrow NO + O_2^+$	2.40e+13	0.41	3.26e+4	$T_{tr}$		Park <sup>18</sup>	N/A
18	$O + O \leftrightarrow O_2^+ + e^-$	7.10e+02	2.7	8.06e+4	$T_{tr}$		Park <sup>20</sup>	1
19	$O + e^- \leftrightarrow O^+ + 2e^-$	1.0e+33	-3.78	1.585e+5	$T_{ve}$		This Work	0.26
20	$O_2^+ + N \leftrightarrow O_2 + N^+$	8.70e+13	0.14	2.86e+4	$T_{tr}$	$T_{tr}$	Park <sup>18</sup>	1
21	$O_2^+ + N_2 \leftrightarrow N_2^+ + O_2$	9.90e+12	0.0	4.07e+4	$T_{tr}$	$T_{tr}$	Park <sup>18</sup>	1
22	$O_2^+ + O \leftrightarrow O^+ + O_2$	4.00e+12	-0.09	1.80e+4	$T_{tr}$		Park <sup>20</sup>	1
23	$O_2 + e^- \leftrightarrow O_2^+ + 2e^-$	2.19e+10	1.16	1.30e+5	$T_{ve}$		Teulet et al. <sup>21</sup>	N/A

## C. Non-Boltzmann Model for NO

The non-Boltzmann rate model applied in this work for NO is a modified version of the models presented by Gorelov et al.,<sup>22</sup> Li et al.<sup>23</sup> and Park.<sup>14</sup> Table 7 presents the electronic levels required for the non-Boltzmann modeling of NO, along with the band system associated with each level and the radiative lifetime. The lower level for each of these band systems is X<sup>2</sup>II.

The coefficients for the excitation rates applied in this work are listed in Table 8. The rates are computed from these coefficients using the following equation:

$$K_{f,ij}^{ex} = A_{ex} T_a^0 .773 \exp(-E_{ex}/T_a) \quad (26)$$

where  $T_a = (T_{ve} T_{tr})^{1/2}$ . Electron-impact processes were found to be negligible for conditions where NO radiation is important, which typically occurs below 10 km/s.

The rates in Table 8 were chosen to obtain the best possible agreement with a range of EAST measurements<sup>24</sup> in the 200 - 230 nm wavelength range. The experimental conditions considered for these comparisons are listed in Table 9. The contribution from each NO band system to the radiance between 200 - 230 nm is shown in Fig. 18 for the 8 km/s, 0.2 Torr case.

Table 7: Electronic levels treated in the present non-Boltzmann model.

$i$	Term	$E_{e,i}$	$g_{e,i}$	Upper Level for:
1	$X^2\Pi$	0	4	-
2	$a^4\Pi$	38807.0	8	-
3	$A^2\Sigma^+$	43965.7	2	$\gamma$ ( $2.6\text{e-}7\text{ s}^{-1}$ )
4	$B^2\Pi$	45932.3	4	$\beta$ ( $5.3\text{e-}7\text{ s}^{-1}$ )
5	$C^2\Pi$	52179.8	4	$\delta$ ( $1.2\text{e-}8\text{ s}^{-1}$ )
6	$D^2\Sigma^+$	53084.7	2	$\epsilon$ ( $4.0\text{e-}8\text{ s}^{-1}$ )
7	$B'^2\Delta$	60364.2	4	$\beta'$ ( $8.9\text{e-}8\text{ s}^{-1}$ )
8	$E^2\Sigma^+$	60628.8	2	$\gamma'$ ( $5.1\text{e-}8\text{ s}^{-1}$ )

Table 8: Heavy-Particle excitation rates ( $\text{cm}^3/\text{s}$ ) for non-Boltzmann modeling applied in the present study.

#	Reaction	$A_{ex}$	$E_{ex}$
1	$\text{NO}(X^2\Pi) + \text{M} \leftrightarrow \text{NO}(a^4\Pi) + \text{M}$	2.51e-6	55858
2	$\text{NO}(a^4\Pi) + \text{M} \leftrightarrow \text{NO}(A^2\Sigma^+) + \text{M}$	5.59e-8	7430
3	$\text{NO}(A^2\Sigma^+) + \text{M} \leftrightarrow \text{NO}(B^2\Pi) + \text{M}$	4.98e-7	2830
4	$\text{NO}(B^2\Pi) + \text{M} \leftrightarrow \text{NO}(C^2\Pi) + \text{M}$	1.25e-6	8990
5	$\text{NO}(C^2\Pi) + \text{M} \leftrightarrow \text{NO}(D^2\Sigma^+) + \text{M}$	6.25e-7	1300
6	$\text{NO}(D^2\Sigma^+) + \text{M} \leftrightarrow \text{NO}(B'^2\Delta) + \text{M}$	2.51e-6	10500
7	$\text{NO}(B'^2\Delta) + \text{M} \leftrightarrow \text{NO}(E^2\Sigma^+) + \text{M}$	6.25e-7	381

Figure 19 compares the measured and simulated radiance integrated between 200 - 230 nm and between  $\pm 1$  cm from the profile peak. Because the non-Boltzmann rates were chosen to match the measurements, the agreement between the non-Boltzmann results and the measurements is good. The simulated result assuming a Boltzmann distribution is also shown in this figure, which is considerably higher than the measurement and non-Boltzmann result, indicating the impact of the non-Boltzmann model.

Figure 20 presents the spatial nonequilibrium profile for each of the cases. The most notable disagreement is seen in the equilibrium plateau for the 9.65 and 10.0 km/s cases. The larger equilibrium value seen for the measurement is likely due to carbon contamination, which results in significant atomic photoionization in this wavelength range. The present analysis therefore assumes that contamination does not significantly influence the nonequilibrium region.

Table 9: EAST Measurements considered in this work.

Velocity (km/s)	Pressure (Torr)	Shot #
8.00	0.2	50-46
8.30	0.2	50-42
8.79	0.2	50-39
9.00	0.2	50-37
9.65	0.2	50-3
10.0	0.2	50-11

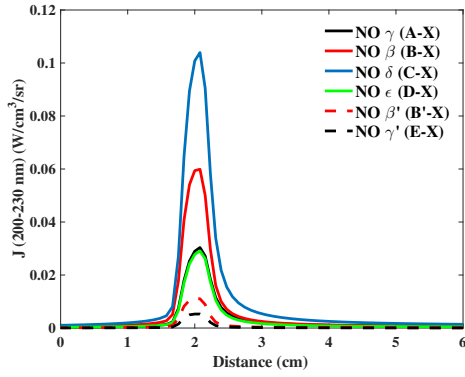


Figure 18: Contribution from each NO band system to the radiance between 200-230 nm.

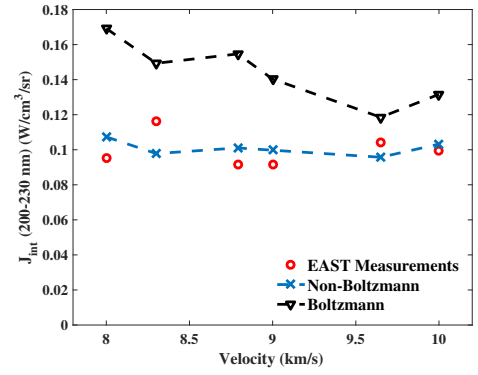


Figure 19: Comparison between simulated and measured radiance values integrated between  $\pm 1$  cm from the profile peak.

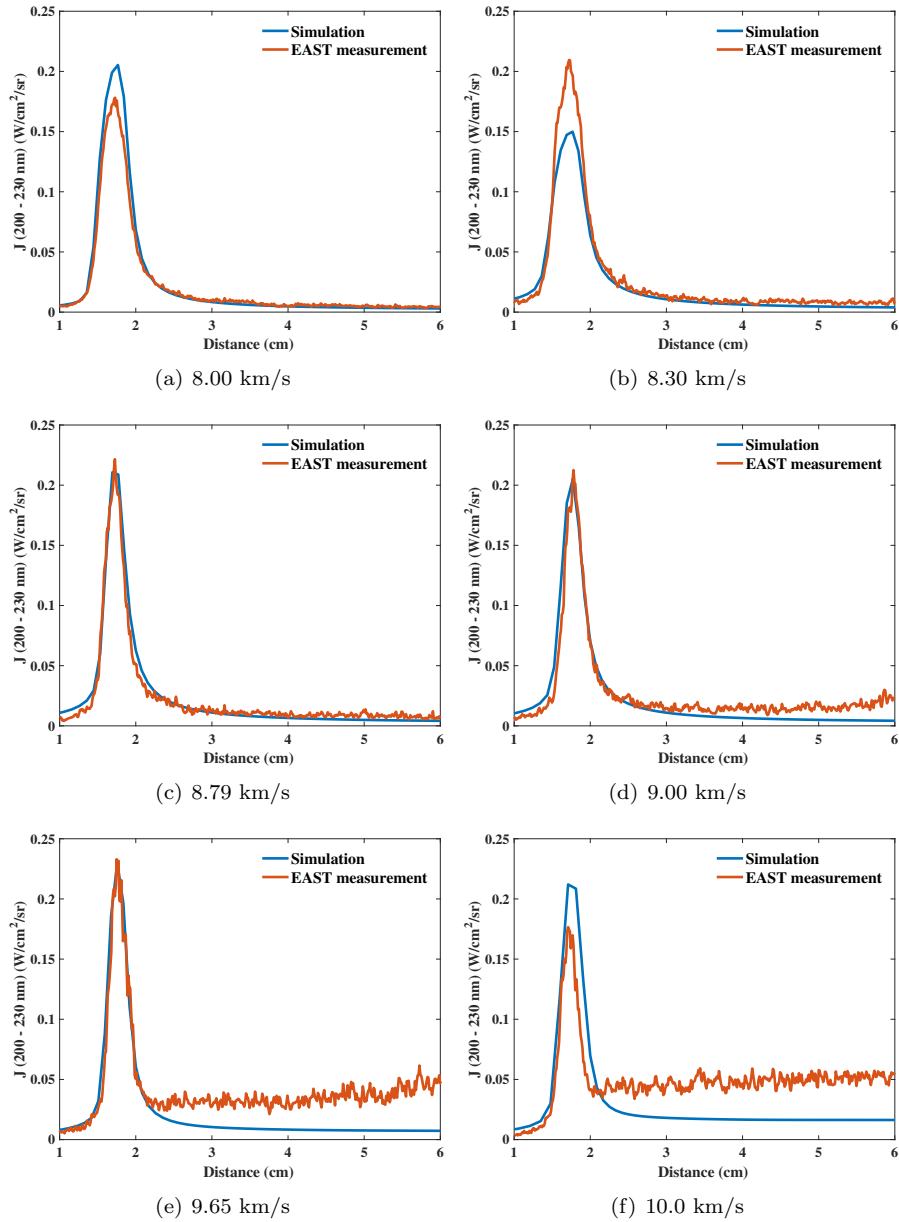


Figure 20: Comparison between simulated and measured nonequilibrium radiance profiles.